Robotica (2011) volume 29, pp. 667–681. © Cambridge University Press 2010
doi:10.1017/S0263574710000548

A humanoid robot capable of carrying heavy objects

Hyeung-Sik Choi†,*, Wonhyun Na‡ and Dongwan Kang§

†*Korea Maritime University, Division of Machanical and Information Engineering College, 1 Dongsam-dong Yeongdo-gu, Busan, Korea*
‡*Hyundai Rotem Company. E-mail: the1stdiv@hotmail.com, Sam-dong Uiwang-city, Kyungki-do, Seoul, Korea*
§*Samsung Machine Tool Engineering Company. E-mail: nims1894@hotmail.com, Gasul-ri, Changwon-city, Korea*

(Received in Final Form: August 11, 2010. First published online: September 10, 2010)

SUMMARY

A new type of 28-DOF (degree of freedom) full-size humanoid robot, driven by a closed-chain type of joint actuation system, is developed in this paper. Each leg of the robot is composed of six joints, where three are at the hip, one is at the knee, and two are at the ankle. The robot has six joints for each arm, one balancing joint, and three joints for the head, with two cameras. The weight of the robot is 75 kg, and its height is 168 cm.

The actuation systems of the pitching joint for the arms and legs of the robot are designed based on a closed-chain mechanism composed of four bar links driven by a ball screw, and each leg of the robot is designed to support 95 kg weight to include a 20 kg payload that can be carried by the robot arms having very light designs (with weight 8.5 kg), but each capable of carrying a 10 kg payload.

An analysis of the closed-chain joint actuation systems of a light arm capable of handling heavy objects is performed, and the light arm is designed via finite-element method analysis performed using ANSYS. In addition, the kinematic analysis and the detailed structure of the arm and leg of the robot are performed.

The main controller uses the ARM processor and a distributed controller for the leg joints is developed using the TMS320c2407 processor with the communications between the main and joint controllers being performed via the CAN system.

Good performances of the proposed robot is demonstrated by presenting several experimental results; these include (1) experimentally handling a 13 kg payload, (2) through walking experiments of the robot supporting a 85 kg load, and (3) measurements of the arm and leg joint motors while performing walking experiments.

KEYWORDS: Humanoid robots; Design; Control of robotic systems; Sensor or actuator design; Bipeds.

1. Introduction

Much research has been undertaken on humanoid robots, these include the P3 robot, developed by Hirai *et al.* at the Honda Company Ltd., as the first human-sized but much heavier robot[1] and Asimo is one of the most advanced medium-sized humanoid robots capable of running and performing various motions.[2] A similar humanoid robot to Asimo are the HRP I and the HRP II robots[3,4], where the HRP II is a slimmer and lighter design, but requires more power to support its body than the HRP I. Another medium-sized humanoid robot, the KHR II, has been developed by the academic institute, Korea Advanced Institute of Science and Technology.[5] All these robots have been developed as humanoids, and they have been designed to walk in a similar manner as human beings. The weights of these latest medium-sized humanoid robots such as Asimo, HRP II, and KHR II are around 50 kg.

Humanoid robots such Asimo, HRP II, and KHR II have been designed to be as light as possible in order to have the minimum weight in their joints since the capacity of the actuating motors is quite limited. To enhance the performance of humanoid robots, an important factor in the structure of their arms and legs is the design of the joint actuation systems so that it is as light as possible but also to transmit high torques or forces. There have been previous research studies on the joint actuation systems that have attempted to increase the torque of the robot. Pneumatic artificial muscles have been presented with high power-to-weight ratios, but these have the problem of being difficult to control, and they are also noisy.[6] Parallel joint actuation systems have enhanced the joint torques but have very limited ranges of motion.[7] For example, a closed-chain joint actuation system has been developed and applied to a robot manipulator, and this has been shown to have three times higher torque transmission and accuracy, though it had a narrower range of motions compared to conventional joint actuation systems composed of motor with harmonic drives or RV speed reducers.[8] Besides these, a number of new actuation systems have been studied, but none show better performance than the conventional joint actuation system.

In this paper, a humanoid robot with a closed-chain type of joint actuation systems is presented; the primary focus is on the closed-chain joint actuation systems, which transmits high torques, and the performance capability of the robot, when carrying a heavy payload, even though its joint actuating power is similar to that of Asimo, HRP II, and KHR II. Through walking experiments of carrying a 15 kg payload, the superior performance of the new developed robot is verified.

* Corresponding author. E-mail: hchoi@hhu.ac.kr

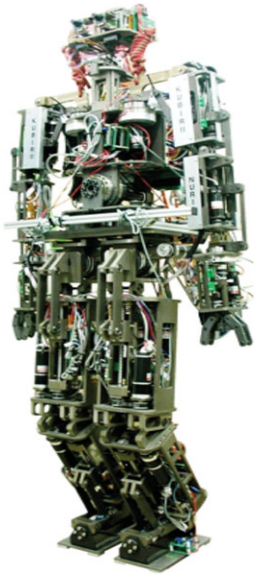

Fig. 1. The developed 28 DOF robot.

2. Design of the Humanoid Robot

2.1. Composition of the robot

In this paper, as shown in Fig. 1, research is undertaken on a 28-DOF (degree of freedom) humanoid robot, with leg joints actuated by a new closed-chain joint actuation system using a four-bar-link mechanism to enhance the robot's performance for carrying heavy payloads. The legs are designed to support heavy weights, and a very light dual robot arm is designed to handle heavy payloads. The humanoid robot is composed of three sections, which are the head, dual arms, and the legs. The specification of the robot is described in Fig. 1, and the outlook of the developed head is shown in Fig. 2. The forward kinematic analysis of the 2 DOF head is performed using the Denavit-Hartenberg (D-H) method,[9] and the transformation matrices are described in the Appendix.

2.2. Design and kinematic analyses of the dual robot arm

As shown in Fig. 3, the dual robot arm is composed of two identical robot arms, and each arm has six joints composed of 2-DOF wrist joints, one elbow joint, 2-DOF shoulder joints, and a gripper joint. The total length of the arm is 75 cm where the link length between the joints of the elbow and shoulder, and that between the joints of the wrist and elbow are 24 cm, respectively. The link length between the joints of the gripper and wrist is 22 cm, and the length of the gripper is 5 cm. The weight of the dual arm is 17 kg.

In the structure of the developed robot arm, a closed-chain mechanism based on a four-bar-link structure (see Fig. 4) is applied to the pitching joint actuation system, which shows superior performance in transmitting torque compared to industrial robot arms.[8] The closed-chain actuation system based on the four-bar-link mechanism is applied to the three pitch joints and the gripper of the robot arm, which are affected by gravity, as shown in Fig. 5. The closed-chain joint actuation system is composed of three rotating links, b_1, b_2, b_3, and one prismatic link composed of a ball screw, which generates a moment force around the rotational joint axis of the robot arm.

The merit of the proposed joint actuation system is that it can generate higher joint torques than the conventional ones by generating a moment, which is caused by the actuating force along the ball screw direction, multiplied by the normal distance between the joint axis of the link and the force vector, as the moment wrench operation is generated. Therefore, the moment can be increased according to the increase of the actuating force, which is related to the lead length or the capacity of the motor, and is also related to the length of the normal distance between the force vector and the joint of the robot arm, which depends on the design of the four-bar-link actuation system. In contrast, the joint actuation systems of most robots are composed of motors with directly coupled speed reducers, such as harmonic drives. This merely generates torque in the same way as a driver device and is the reason why the four-bar-link joint actuation system can have heavier payloads than conventional joint actuation systems. The rotating speed of the joints can be slower than that of conventional joint actuation systems, but this speed of rotation can be increased by simply exchanging the ball screw with longer leads. The superior torque transmission of the proposed joint actuation system is verified through experiments on the robot arm of 60 and 18 W joint motors of small power, by lifting a 10 kg load. It is worth noting that the total weight of one robot arm is only 8.5 kg.

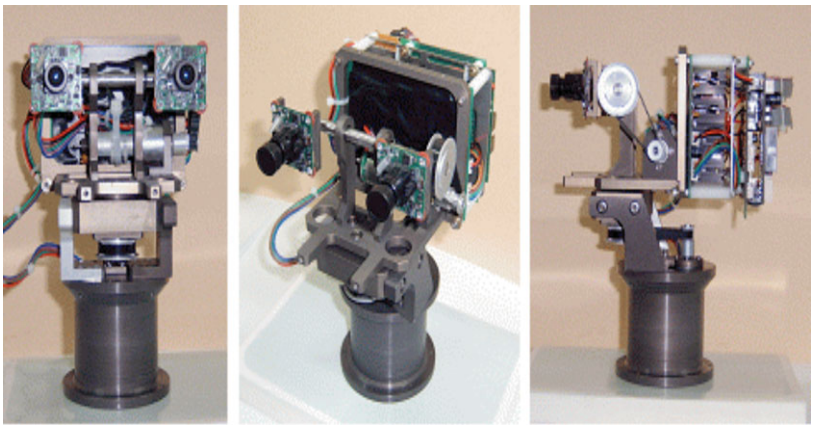

Fig. 2. Front and side views of the head.

https://doi.org/10.1017/S0263574710000548 Published online by Cambridge University Press

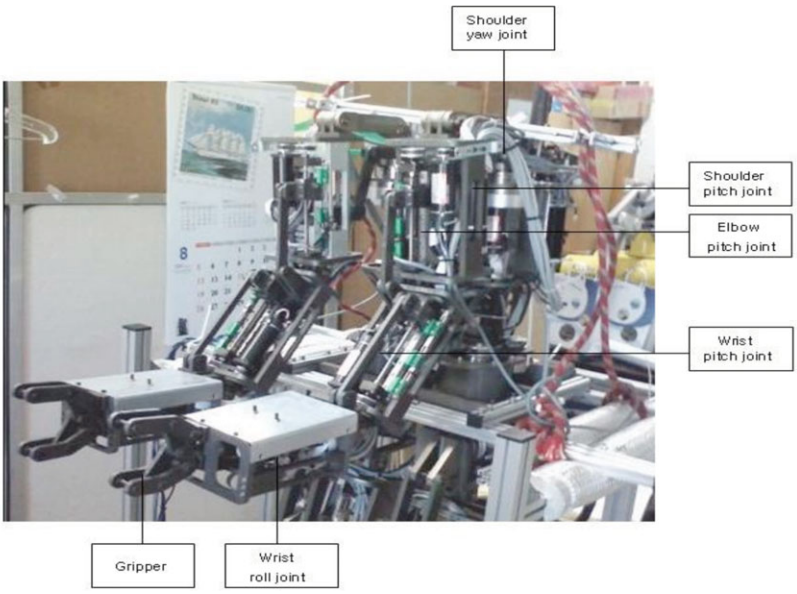

Fig. 3. Appearance of the developed robot arm.

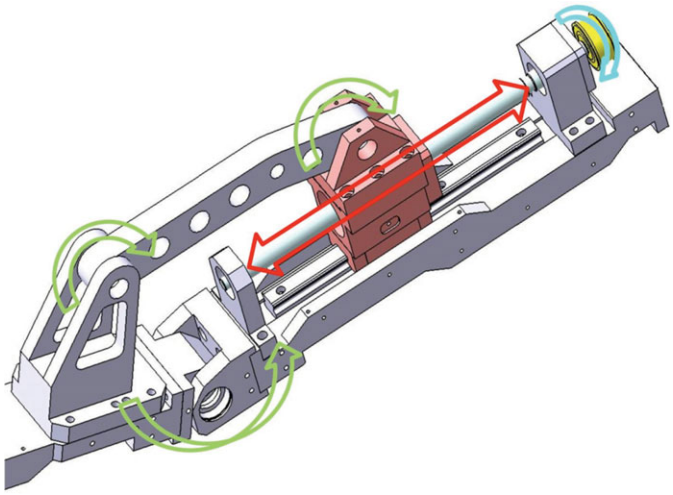

Fig. 4. Structure of the four-bar-link actuation system.

A kinematic analysis of the lightweight 12-DOF dual robot arm is performed to identify the joint angles corresponding to the position of the gripper in Cartesian coordinates. Since the robot arm has two 6-DOF identical arms, the kinematic and inverse-kinematic analyses on one arm can be performed. To do this, first, a homogeneous transformation matrix of the position and orientation of the gripper is defined with respect to the origin through the kinematic analysis.

For the purpose of the kinematic analysis, the D-H notation is used to establish the coordinate system on each joint, as shown in Fig. 6, and Table I shows the D-H link parameters used in the analysis according to the established coordinates.

Substituting the parameters in Table I into the homogeneous transformation matrix in the Appendix in sequence for $i = 1, 2, 3, 4, 5$, the kinematic relationship between the end point of the gripper in Cartesian coordinates and joint angles can be obtained as

Table I. Parameters of the robot arm.

Link	a_i	α_1	d_i	θ_i
1	a_1	90	0	θ_1
2	a_2	0	0	θ_2
3	a_3	0	0	θ_3
4	0	90	0	θ_4
5	0	0	d_5	θ_5

$a_1 = 141$ mm, $a_2 = 240.35$ mm,
$a_3 = 231$ mm, $d_5 = 235.06$ mm.

$$T_0^5 = A_1 A_2 A_3 A_4 A_5 = \begin{bmatrix} r_{11} & r_{12} & r_{13} & P_x \\ r_{21} & r_{22} & r_{23} & P_y \\ r_{31} & r_{32} & r_{33} & P_Z \\ 0 & 0 & 0 & 1 \end{bmatrix}. \quad (1)$$

The components are described in the Appendix. The specifications of the actuating motors applied on the joints of the robot arm are listed in Table II.

2.3. Analysis on the torque applied by the joint actuation system

The capacity of the motor applied to the four-bar-link structured joint can be computed with the related equations of the force distribution applied on the joint actuation system. Eqs. (2)–(4) illustrating the force distribution relations between the sum of the robot's weight and the external load and the force applied on the ball screw actuation system are substituted into Eq. (5) to determine the value of the torque that is exerted on the motor. The calculated torques exerted on each joint are compared with the torque performances of the actual motors applied in the robot to verify the validity of the joint actuation system design.

https://doi.org/10.1017/S0263574710000548 Published online by Cambridge University Press

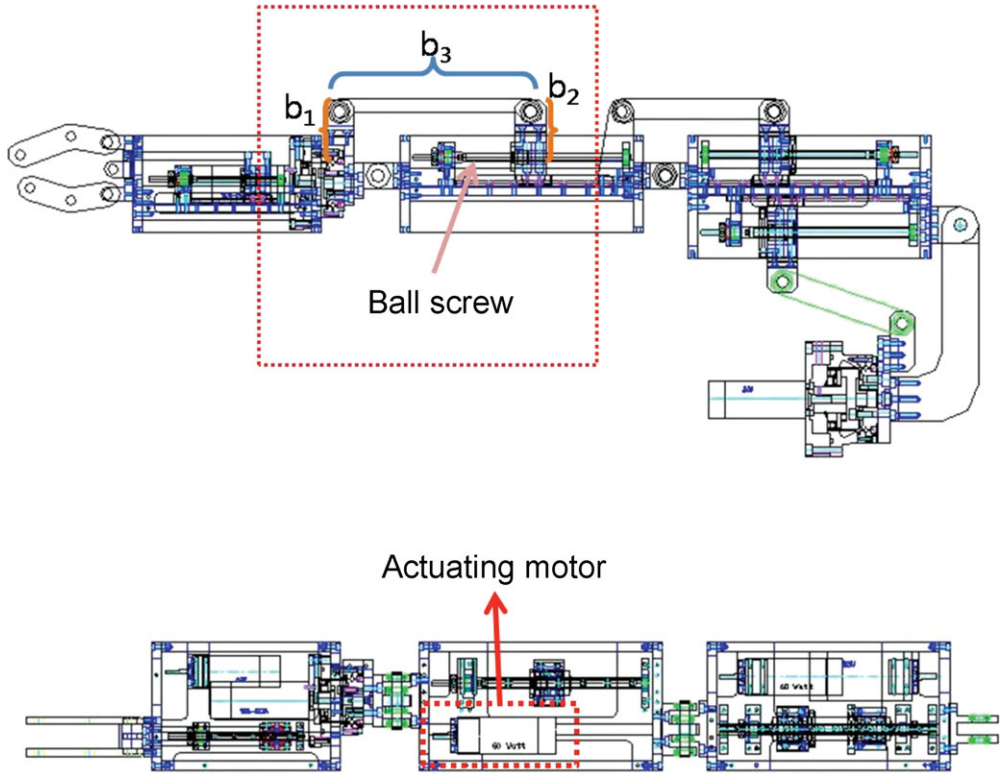

Fig. 5. Computer-aided design of the robot arm with the four-bar-link actuation system.

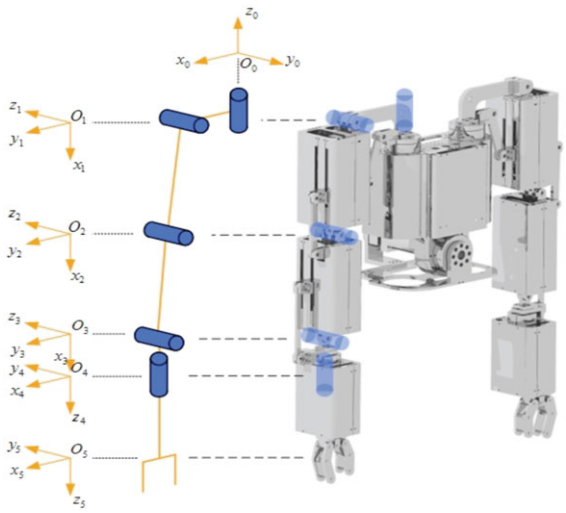

Fig. 6. Coordinates of the arm.

Geometric mapping has been performed, as shown in Figs. 7–9 to derive the equations of the load torques of each link actuation system. To simplify the analysis, the external forces that generate the moments have been vector-transferred along the same directions of the ball screws. The length of the ball screws and the joint angles θ_{i1} in the four-bar-link joint is varied when the robot arm is in motion. Thus, the magnitude of the external force F_i in the direction of the ball screw axis also changes.

As illustrated in Fig. 7, a geometric mapping has been performed for the force distribution analysis of the shoulder joint, which operates in the roll motion vertically to the direction of gravity. Therefore, a force distribution analysis regarding the shoulder weight M_1 has been illustrated by taking into consideration the pushing and pulling characteristics of the load on the shoulder joint motor.

The figure illustrating the force distribution relationship of the elbow joint is identical to that seen in Fig. 8, and the applied load M_2 is the force generating a torque on the elbow joint of the robot.

The wrist joint is also of the same structure as the shoulder joint. Thus, the figure illustrating the force distribution relationship of the joints is identical to that shown in Fig. 9 where the load M_3, which is only applied to the wrist joint,

Table II. Specification of the joint actuation system.

Axis	Joint structure	Motion	Motor capacity [W]	Pulley ratio	Ratio of speed reducer	Ball screw lead [mm]
0	Directly connected	Yaw	60	–	1:160	–
1	Four-bar-link	Pitch	150	1:2	1:4.3	2
2	Four-bar-link	Pitch	60	1:2.5	–	2
3	Four-bar-link	Pitch	60	1:2.5	–	2
4	Directly connected	Roll	60	–	1:100	–
5	Four-bar-link	Gripper	18	1:3	–	2

https://doi.org/10.1017/S0263574710000548 Published online by Cambridge University Press

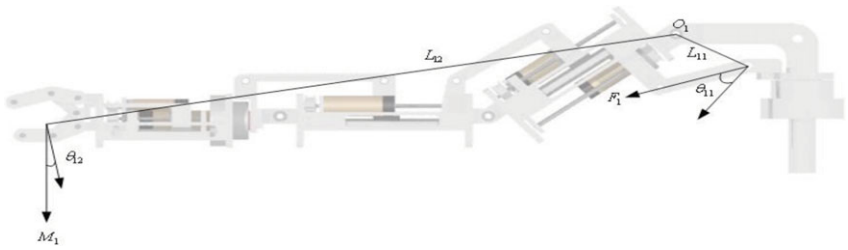

Fig. 7. Torque analysis of the shoulder joint.

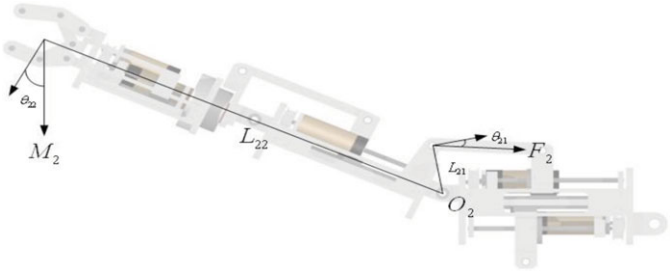

Fig. 8. Torque analysis of the elbow joint.

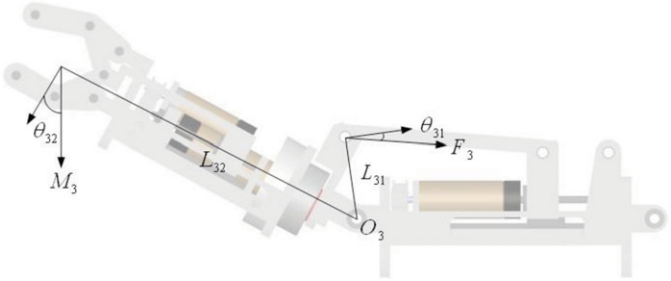

Fig. 9. Torque analysis of the wrist joint.

serves as the force for generating a torque on the wrist joint of the robot.

Herein, M_i represents the sum of the robot's weight and external payload applied to the robot. When a 10 kg payload is applied to the gripper of the robot arm, M_1 is 16.2 kg, M_2 is 13.3 kg, and M_3 is 11.9 kg for the proposed robot arm. To be able to support the weight exerted on the robot arm, and the external load, an equation for analyzing the capacity of the driving motor applied on the closed-chain joint actuation system is derived. For this, the related equation of each joint unit and the torque regarding the external force has been determined in the following manner, from the sum of moments about the axis of rotation O_i illustrated in Figs. 7–9.

$$F_1 = \frac{M_1 L_{11} \cos\theta_{12}}{L_{12} \cos\theta_{11}}, \tag{2}$$

$$F_2 = \frac{M_2 L_{22} \cos\theta_{22}}{L_{21} \cos\theta_{21}}, \tag{3}$$

$$F_3 = \frac{M_3 L_{31} \cos\theta_{32}}{L_{31} \cos\theta_{31}}. \tag{4}$$

Equation (5) represents a relation between the load applied along the ball screw of the four-bar-link joint actuation system and the torque of the actuating motor of the ball screw.

Table III. Properties of joint actuator of robot arm.

Joint	Lead of ball screw l_b [mm]	Efficiency of screw η [%]	Motor Max. continuous torque [Nmm]
Shoulder	2	90	181
Elbow	2	90	94.8
Wrist	2	90	94.8

$$\tau_{i(\text{Motorload})} = \frac{F_i l_b}{2\pi\eta A}, \tag{5}$$

where F_i indicates the applied force along the ball screw, l_b indicates the lead of the ball screws, η indicates the efficiency of the ball screw, and A indicates the gear ratio of the motor. Table III presents the properties of the actuation systems including the motor applied to the closed-chain actuation system. Herein, Maxon motors rated at 150, 60, and 60 W were applied to the shoulder, elbow, and wrist joints composed of the four-bar-link mechanism, respectively.

By using the force distribution Eqs. (4)–(7), the relation between the torque applied to the joint motor with respect to the configuration of the joint angles has been simulated, and the simulation results of the motor torque within the rotating angle range of the shoulder joint is presented in Fig. 10; those of other joints can be similarly illustrated.

Figure 10 illustrates the results derived from the relation between the force distribution Eqs. (2) and (5) within the working space $-6°$–$30°$ of the shoulder joint. Herein, the

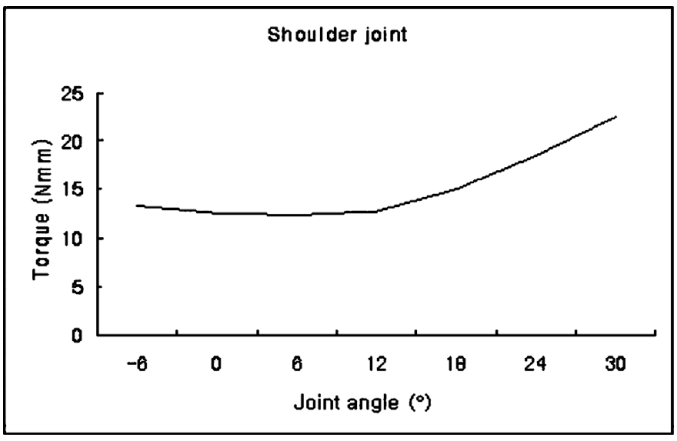

Fig. 10. Applied torque to the shoulder joint motor.

https://doi.org/10.1017/S0263574710000548 Published online by Cambridge University Press

Table IV. Property of aluminium.

	Modulus of elasticity (GPa)	Intensive stress (MPa)	Density (kg/m^3)
AL6061	68.9	225	2710

Table V. Elements and nodes of model.

	Type of elements	Number of elements	Number of nodes
Body	SOLID	104,642	283,229
Links	BEAM	360	691

minus sign represents the rotation to the inner side of the body. According to the simulation results, when the shoulder joint is 30°, a maximum torque 24 Nmm is loaded to the driving motor of the shoulder joint. This is less than 1/7 of the maximum continuous torque 181 Nmm of the driving motor, as specified in Table III, which indicates that the actuation system designed has enough torque to carry loads heavier than the external load of 10 kg on the robot's gripper.

By performing similar simulations on the motor torque of the elbow joint applying the relation between the force distribution Eqs. (3) and (5) within the working space 0°–70°, a maximum torque of 72 Nmm is loaded at 0° when the robot arm is horizontally positioned. Since the maximum loaded torque of 72 Nmm is less than the maximum continuous torque of 94 Nmm of the actuator motor, it is indicated that the actuation system of the elbow joint is designed to allow loads heavier than external loads of 10 kg applied to the robot's gripper. Also, for the wrist joint motor, within the wrist joint's rotating angle range of 0°–35°, a maximum load torque of the wrist joint is 19.5 Nmm, which occurs when the wrist joint aligns with the link of robot arm. The maximum loaded torque is less than the maximum continuous torque of the actuator motor, which indicates that the actuation system of the wrist joint is designed to allow a load heavier than the external load of 10 kg to be applied to the robot's gripper.

2.4. FEM analysis for designing the lightweight robot arm

For developing a light robot arm, the weight of the link, including the actuation systems, should be light. Because of the superior performance of the four-bar-link actuation system, small and light actuating motors can be applied to the robot arm. For designing a lightweight robot link with minimal deflections, a computer simulation based on the FEM method has been performed.

In this paper, the computer simulation based on the FEM method has been performed using ANSYS, where the links of the robot arm are modeled using solid elements, and links connecting the joints and the gripper are modeled using beam elements. In the FEM analysis, the property of aluminium (AL6061) for the robot arm has been used; these properties of aluminium are presented in Table IV, and the number of elements and nodes are presented in Table V.

In the simulation for designing the robot link, the payload of 10 kg is applied at the midpoint of the gripper. Under these conditions, the deflection of the end point of the gripper is calculated using ANSYS. The thickness of the robot link is 10 mm in the FEM analysis, which is the same as that of the actual robot arm. Then, the weight of the robot arm including the actuation systems, becomes around 8.5 kg, which is very light compared with the 10 kg payload. Under these conditions, the deflections of the end point of the gripper, wrist, elbow, and shoulder joint can be calculated.

Results of FEM analysis on the deflection of the robot arm are presented in Table VI and in Fig. 11, the results of the FEM analysis to represent the variation of the deflection of the whole link is shown, where the parts of the link are sectioned by colors, where the most deflected point (the end point of the gripper) is noted by the red color. Also, on the right side, the deflections of the colored sections are described.

As already stated the payload capacity of each arm in the proposed dual robot arm is designed to support a 10 kg payload; when this is compared with other light robot arms applied to humanoids or mobile robots, the load capacity is much bigger since most of the others can only handle less than about 1 kg load, and the heaviest load ever reported being held is 4.25 kg, by the HRPII robot.[4] The characteristics of the developed robot arm are evaluated in two ways, namely, by the ratio of the payload capacity/robot weight and the repeatability.[7] The weight of the arm and its payload capacity are 8.5 kg and 10 kg, respectively, so that the ratio is 1.18, which is a very high value compared to these ratios for industrial robots. Even though there are relatively high repeatability errors due to deflections of the robot arm, it would be affordable for the humanoid robot performing somewhat inaccurate tasks in normal human environments.

2.5. Analysis on the joint actuation system based on the four-bar-link mechanism

In the proposed robot arm, since the servomotors with encoders are connected to ball screws, the positions of the robot arm are expressed in the prismatic coordinates of the ball screws. However, in order to obtain the inverse kinematic information, the position of the robot arm should be expressed by the joint coordinates. For this, the kinematic relations between the revolute joint and the prismatic joint of the robot arm are analyzed.

Among the six robot joints, the four-bar-link structure is applied to the four joints, except the shoulder joint with yaw motion and the wrist joint with roll motion. The four-bar-link structure has the benefits of being relatively lighter but

Table VI. Deflection of robot links.

Thickness of link (mm)	Links load kg	Wrist (mm)	Elbow (mm)	Shoulder (mm)	Deflection of end point (mm)
10	6.5	0.280	1.274	3.500	8.806

https://doi.org/10.1017/S0263574710000548 Published online by Cambridge University Press

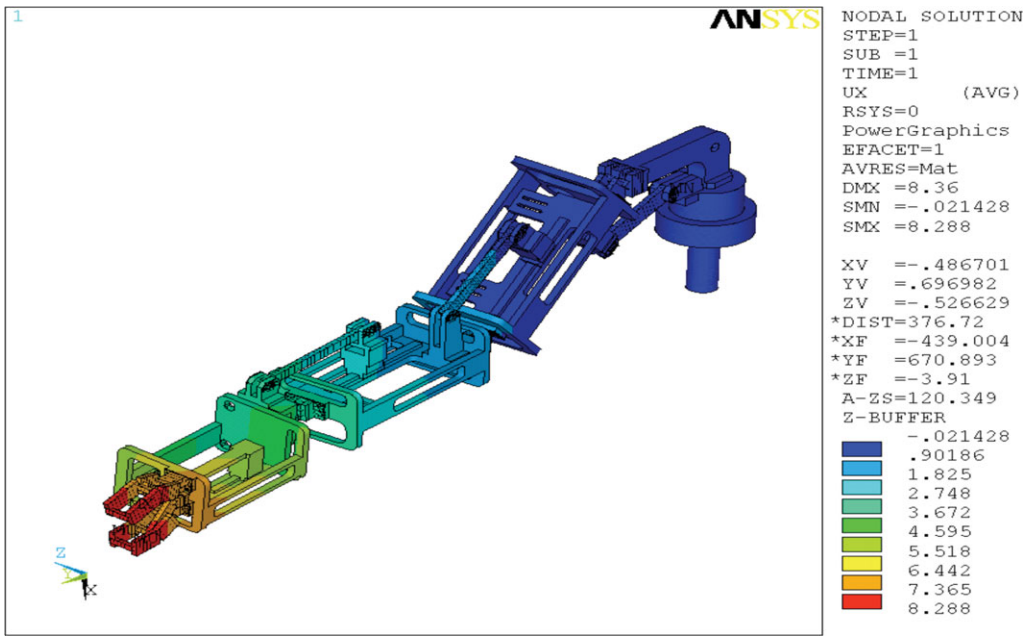

Fig. 11. Deflection of the robot links using ANSYS analysis.

yet able to generate three times higher torque transmission capability and position accuracy than the conventional speed reducer such as the harmonic drive.[8] The relation between the position of the ball screw and joint angle is described in Fig. 12 and is expressed by the following equations. In this paper, only the case of the elbow joint actuation system is analyzed since the other joints have similar structure.

In Fig. 12, the four bar links b_1, b_2, b_3 are related with the rotational joints, and d_2 is related with the prismatic joint. The geometric relation between the joint angle of the elbow, $q$and the prismatic displacement, d of the ball screw aligned along d_2 is shown in Fig. 7, where the equation for the joint angle is expressed as $q = 180^\circ - (\theta_1 + \theta_2 + \theta_3)$. The relation between $q$and d is expressed by the following equations. In Fig. 12, the parameters θ_3, P_2, b_2, b_1 are decided by the design of the robot arm, and d_2 is decided by the measured d since it is aligned along the d_2 direction. Using these, P_2 can be expressed as

$$P_2 = \sqrt{b_2^2 + d_2^2} \tag{6}$$

and θ_1 can be obtained as

$$\theta_1 = a\tan\left(\frac{b_2}{d_2}\right). \tag{7}$$

Using the cosine rule, the following equation can be obtained.

$$P_2^2 + b_1^2 + 2b_1 P_2 \cos\theta_2 = b_3^2. \tag{8}$$

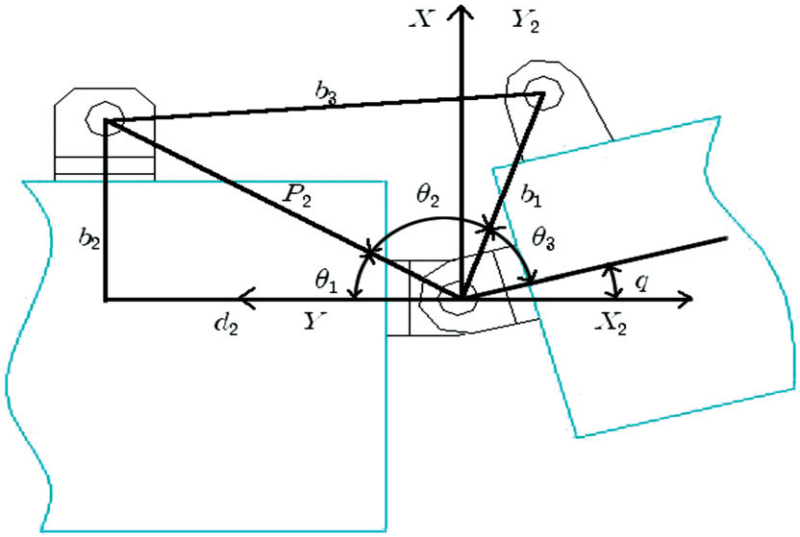

Fig. 12. Four-bar-link structure for the elbow joint.

https://doi.org/10.1017/S0263574710000548 Published online by Cambridge University Press

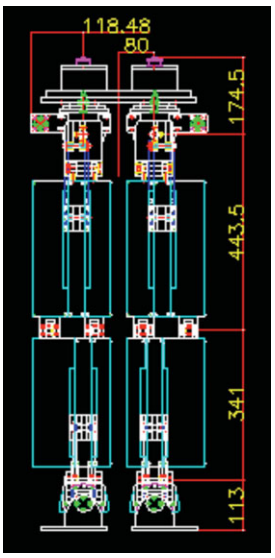

Fig. 13. Dimension and picture of the robot leg.

Finally, θ_2 can be obtained from the equations as

$$\theta_2 = a\cos\frac{b_3^2 - \left(P_2^2 + b_3^2\right)}{2b_1P_2}. \quad (9)$$

In this way, q is expressed as a function of d.

2.6. Design and kinematic analysis of the robot leg

The total length of the leg is 107.2 cm, and its link length is described in Fig. 13. The four-bar-link joint actuation system is applied to the three pitching joints of the pelvis, the knee, and the ankle joints. In the humanoid robot, the torque actuation of the leg joint is most important for supporting and walking. This is the reason why the four-bar-link joint actuation system is applied to the three pitching joints of the proposed robot legs, since the actuation system generates higher torques than that of a conventional joint actuation system composed of the motor and the harmonic drive, which is described in Section 2.3.

A kinematic analysis is performed on the robot leg for the position control of the robot leg. As illustrated in Fig. 14, the coordinates have been installed on all joints of the robot leg using the D-H notation, and the link parameters, obtained through the D-H rule, are listed in Table VII. The robot leg deduces the matrix that demonstrates the position and orientation of the foot from the center of the main body with the use of the transformation matrix presented in the Appendix from the parameters of Table VII.

$$T_{0,leg}^{6} = A_1A_2A_3A_4A_5A_6A_7 = \begin{bmatrix} r_{11} & r_{12} & r_{13} & P_x \\ r_{21} & r_{22} & r_{23} & P_y \\ r_{31} & r_{32} & r_{33} & P_z \\ 0 & 0 & 0 & 1 \end{bmatrix}. \quad (10)$$

Components of $T_{0,\text{leg}}^{6}$ are presented in the Appendix.

The specification of the actuating motors applied on the joints of the robot leg is listed in Table VIII.

Table VII. Link parameters of the robot leg.

Link	a_i	α_i	d_i	θ_i
1	0	90°	d_1	θ_1^*
2	a_2	−90°	0	θ_2^*
3	a_3	0	0	θ_3^*
4	a_4	0	0	θ_4^*
5	a_5	90°	0	θ_5^*
6	a_6	0	0	θ_6^*

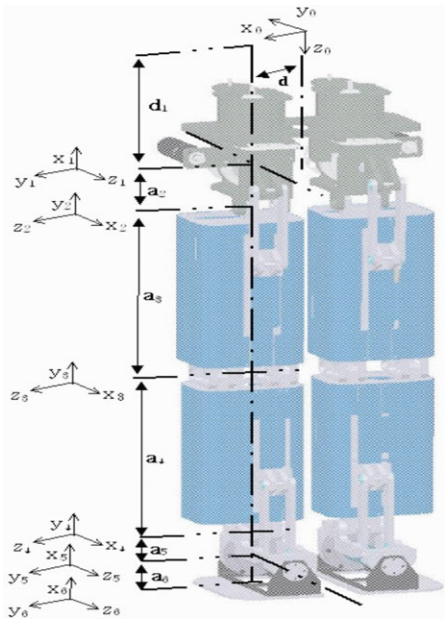

Fig. 14. The coordinate system of the robot leg.

In this paper, the mechanism of the four-bar-link joint actuation system is omitted since the structure of the leg joint actuation systems is similar to the case of the elbow joint actuation system analyzed in Sections 2.3 and 2.5.

3. Control system for the robot

3.1. Composition of control system

For the robot, an entire control system consisting of a host PC, a main controller, and joint motor controllers is developed. The host PC has the role of executing the control algorithm, sending the order of the operational signals to the main controller for the robot arm and monitoring the results of the command signals. The main controller sends the control signals to the joint motor controllers through RS232 communications. The main controller, the ARM Board, is composed to send continuous motion signals to the motor controllers of the joint actuation systems, according to a trajectory-planning scheme. For the joint motion controller, a TMS320c2407 microprocessor is applied. The developed hardware structure of the control system is presented in Fig. 15, where the motion controller for the joint actuation system is shown in Fig. 16. The controller is built in a modular control board capable of controlling two motors and is designed to generate the pulse width modulation (PWM) signals and the directional signal for the motor and

https://doi.org/10.1017/S0263574710000548 Published online by Cambridge University Press

Table VIII. Specification of the joint actuation system.

Axis	Joint structure	Motion	Motor capacity [W]	Pulley ratio	Ratio of speed reducer	Ball screw lead [mm]
0	Directly connected	Roll	150	1:2	1:160	–
1	Directly connected	Yaw	150	1:3	1:160	–
2	Four-bar-link	Pitch	150	1:1	1:1	4
3	Four-bar-link	Pitch	150	1:1	1:1	4
4	Four-bar-link	Pitch	150	1:1	1:1	4
5	Directly connected	Roll	150	–	1:160	–

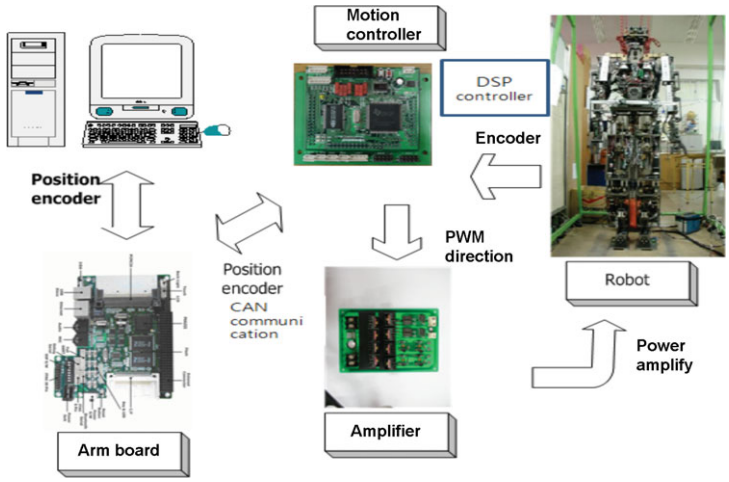

Fig. 15. Composition of the control system.

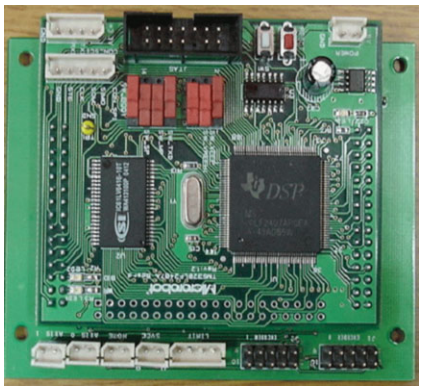

Fig. 16. Outlook of the motion controller.

sends them from the main controller to the motor driver. The motor driver is developed to supply the power, which is proportionally amplified with the required duty ratio to the joint actuating motors according to the PWM signal and the directional signal for the joint motor. The motor driver is developed by composing a bridge circuit with power transistors and is designed to have a time-delay function to protect overcurrents, as shown in Fig. 17

A (proportional-integral-derivative and feed forward) PIDF control algorithm is applied to the joint controller, which is widely used in industry since it affords a fast calculation time and is easy to code. The loop time of the controller is set at 2 ms by using the interrupt function, and the PID control system design is capable of completing the calculation of the control data within that time. In addition to this, in order to compensate for the gravity effects on the robot links, a feed forward force is applied, as shown in Fig. 18. The position controller is applied to the dual arm for testing the arm as it supports the payload.

4. Performance Experiments of the Dual Arm

4.1. Payload experiment of the robot arm

An actual load test is performed with a 13 kg payload applied at the midpoint of the gripper of the dual arm. Figure 19 shows the experimental situation in which a load of 13 kg is applied to the dual robot arm. As shown in Fig. 19, the dual arm is able to support the 13 kg payload successfully. For verification of the payload experiments, the payload current applied to the shoulder joint actuator is measured since the heaviest payload is applied to the shoulder joint. For this, a Hall sensor is used to the joint actuator motor and the measured voltage through the Hall sensor is converted using a 10-bit A/D converter. In the test, the position of the joint angles of the robot arm is controlled using the PIDF control algorithm. For the pitching joint actuation system, a 150 W Maxon motor is applied. Two experiments are performed, and the results are expressed as the solid and the dotted lines: One test is to hold a 13 kg payload (dotted line), and the other is to perform a uplifting motion with the 13 kg payload (solid line), as shown in Fig. 20. According to the measured data, the maximum payload current is about 0.4 A for the holding experiment. For the motion case, uplifting the payload with a slow steady speed of 0.1 rad/s for 0.7 s, and

https://doi.org/10.1017/S0263574710000548 Published online by Cambridge University Press

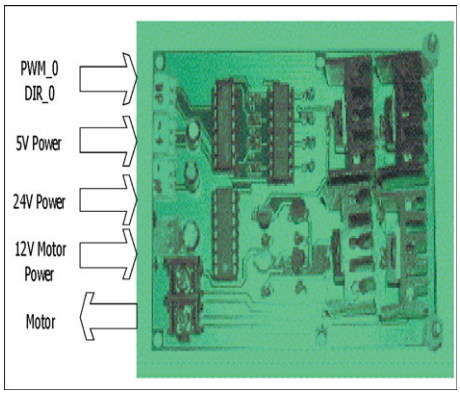

Fig. 17. Outlook of the motor driver.

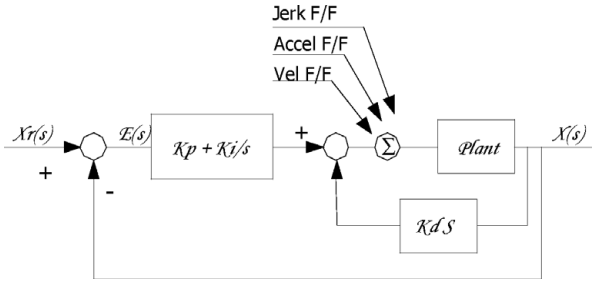

Fig. 18. PID controller with the feed forward term.

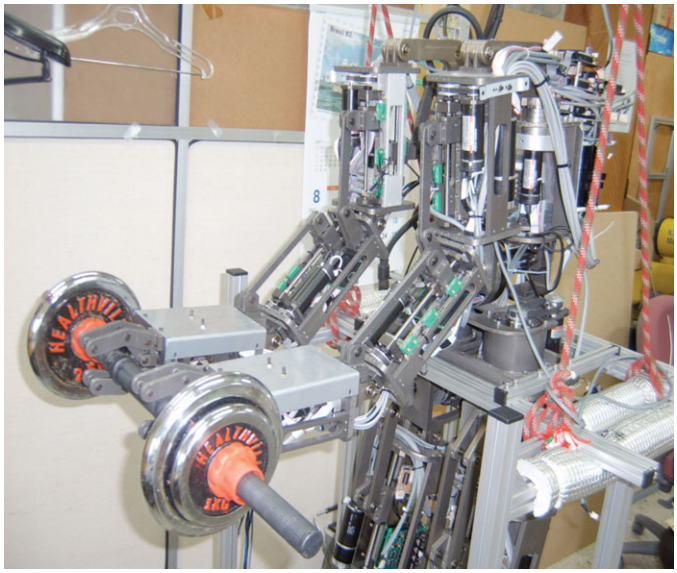

Fig. 19. Payload test of the dual robot arm.

accelerating for 0.1 s for the maximum speed of 0.5 rad/s and decelerating experiments for 0.1 s. The maximum payload current is about 2 A for the motion experiment. Since the continuous maximum current of the 150 W Maxon motor is 6 A, the joint actuation systems have enough capacity for much heavier payloads and faster motions. Through these experiments, the excellent performance of the proposed robot arm with four-bar-link structure is verified.

From the aspect of payload capacity, each arm of the proposed dual robot arm is designed to support a 10 kg payload, which is significantly larger than other light robot

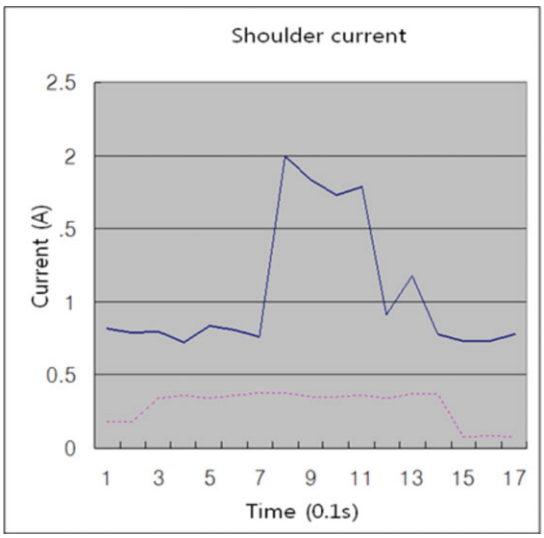

Fig. 20. Load current of the shoulder joint motor.

arms applied to other similar robots where the payloads are normally around 1 kg load.

The weight and the actual payload capacity of the developed robot arm are 8.5 and 10 kg, respectively, so that the value of the payload/robot arm weight ratio is 1.18, which is a very high value compared to those of industrial robots. Some examples of these characteristics of industrial robots are presented in Table IX. It is noted that the developed robot arm has a superior value for the ratio of the payload capacity/robot weight compared to industrial robot arms including scalar robot arms.

5. Walking Test

5.1. Walking algorithm

For the walking test of the robot, eight operational stages of a simple forward walking algorithm and one stop stage are planned, as illustrated in Fig. 21, where the forward walking test is conducted and the results illustrated. The joint angle data of both legs are generated using the simulation of the prespecified eight forward walking stages. Data for the five joints, except the yaw joints, are presented, since these yaw joints do not move during forward walking and the generated data are applied with little modification to the humanoid robot. The successful walking results are shown in Fig. 22, where the robot is carrying a 13 kg payload.

5.2. Walking test of the robot

The load test for the robot walking is performed under 85 kg weight, which is the sum of the robot weight and a payload of 13 kg, without the weight of the head**.** It is shown that the robot is able to walk according to the prespecified trajectory successfully, as shown in Fig. 22. In the experiment, the robot walks according to the eight walking stages, step by step. While performing the walking experiment**,** the load currents applied to the pitching joint motors are measured with a 13 kg payload. For this, Hall sensors are used to monitor the joint actuator motors, and the measured voltages through the Hall sensors are converted using 10-bit A/D converters.

https://doi.org/10.1017/S0263574710000548 Published online by Cambridge University Press

Table IX. Characteristics of robot arms.

Robot	DOF	Length (mm)	Weight (kgf)	Payload (kgf)	Payload/weight
Motoman-IA20	7	1200	120	20	0.16
Puma RS84	4	1200	130	5	0.038
ABB IRB 2000	6	1450	370	10	0.027
Kuka DLRII	7	936 (horizontal: 630)	17	17	1.0
Developed robot	6	750	8.5	10	1.18

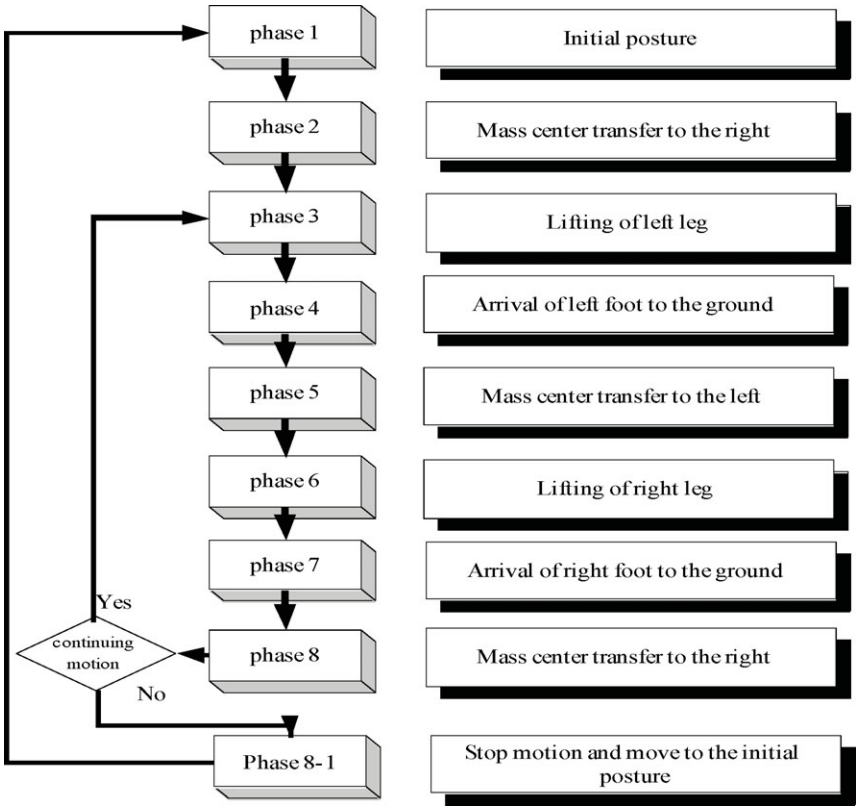

Fig. 21. Steps of the walking motion.

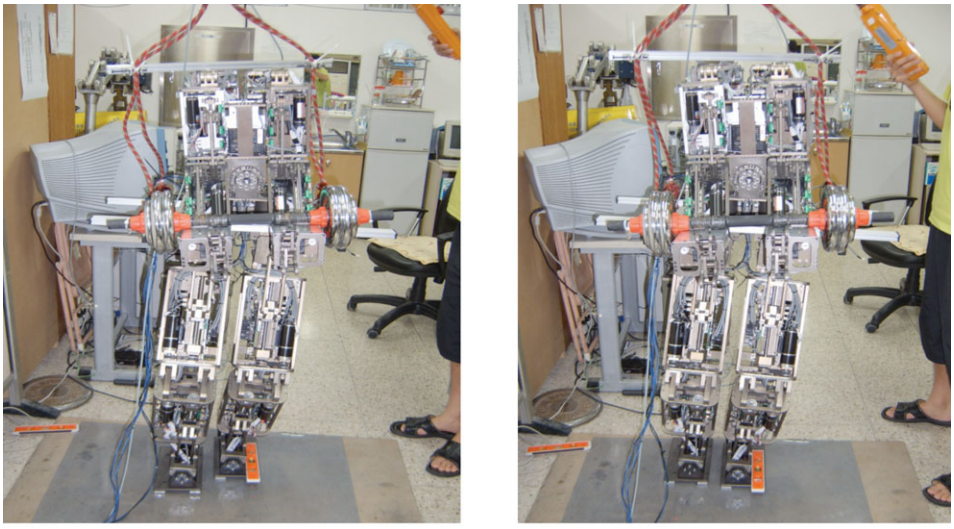

Stage 1 (left leg motion) **Stage 2 (left leg motion)**

Fig. 22. For caption see next page.

https://doi.org/10.1017/S0263574710000548 Published online by Cambridge University Press

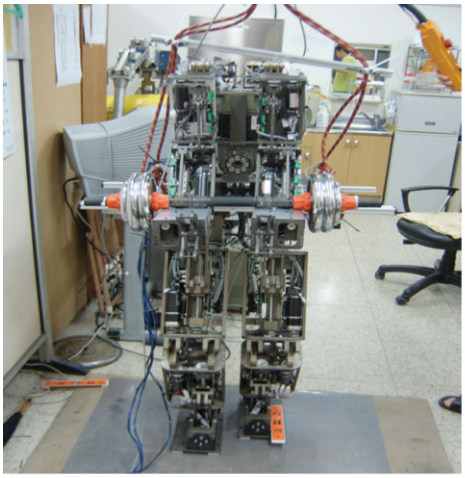

Stage 3 (left leg motion)

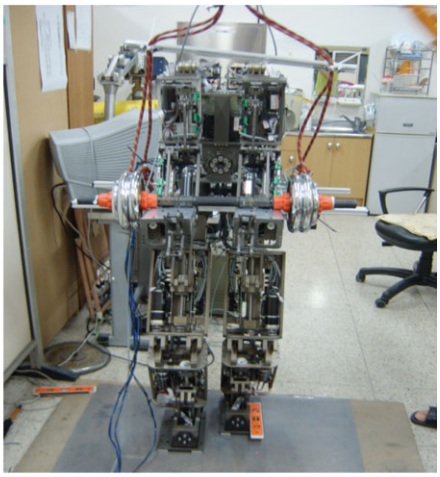

Stage 4 (left leg motion)

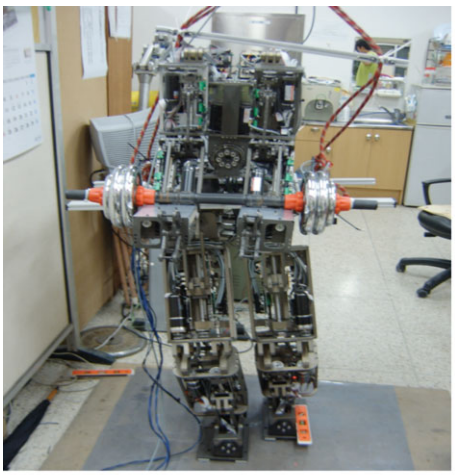

Stage 5 (right leg motion)

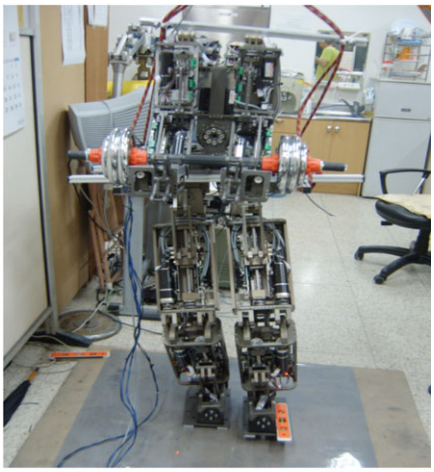

Stage 6 (right leg motion)

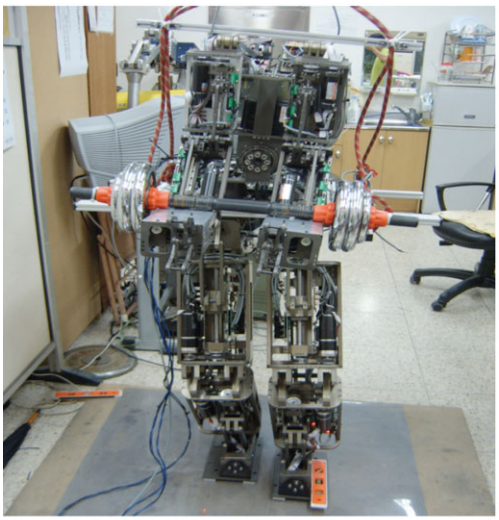

Stage 7 (right leg motion)

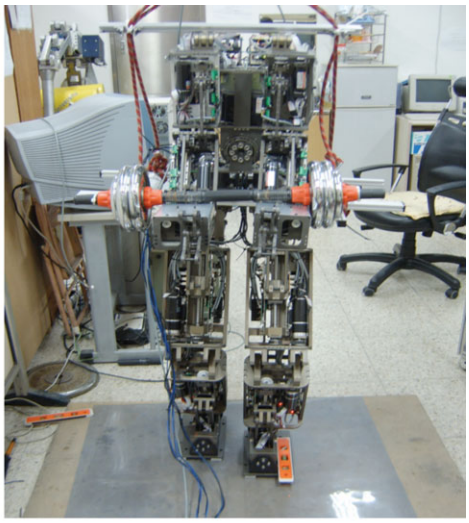

Stage 8 (right leg motion)

Fig. 22. Walking tests of the robot with 13 kg weight. (a) Mass center transfer motion of roll joint in stage 1 (motion time: 0.8 s, maximum current: 1.5 A). (b) Stepping forward motion of pitch joint in stage 2 (motion time: 1.1 s, maximum current: 0.77 A). (c) Stepping-down motion of pitch joint in stage 3 (motion time: 1.1 s, maximum current: 1.05 A).

https://doi.org/10.1017/S0263574710000548 Published online by Cambridge University Press

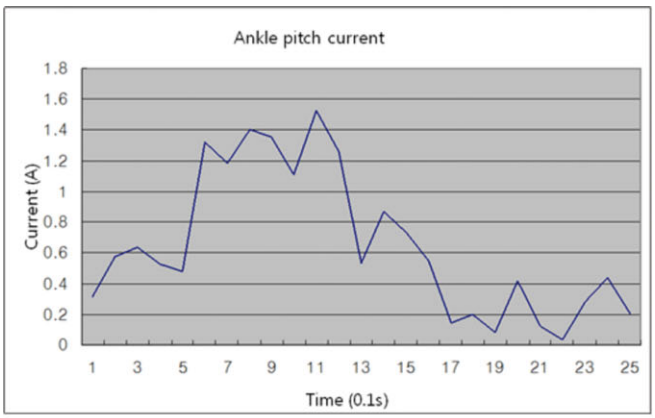

(a) Mass center transfer motion of roll joint in stage 1
(Motion time: 0.8 second, maximum current: 1.5(A))

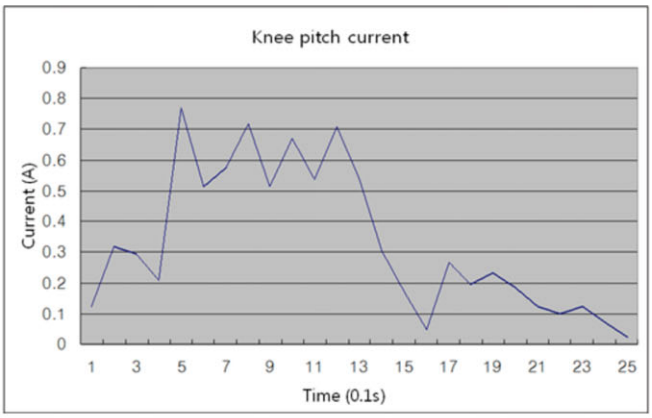

(b) Stepping forward motion of pitch joint in stage 2
(Motion time: 1.1 second, maximum current: 0.77(A))

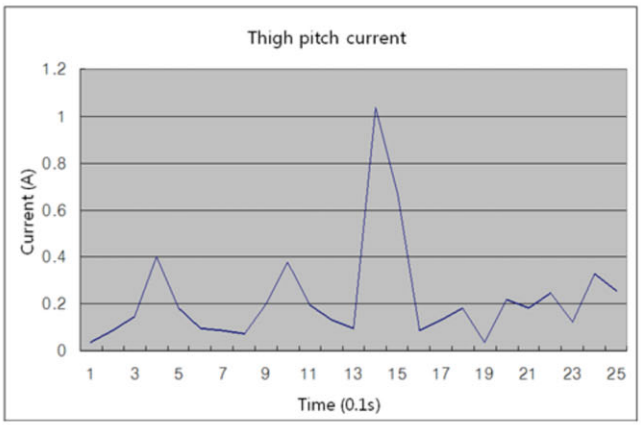

(c) Stepping-down motion of pitch joint in stage 3
(Motion time: 1.1 second, maximum current: 1.05(A))

Fig. 23. Measurement of the torque load in the leg joints.

The measured currents are converted into torques through the related equations between the motor torque and the transverse force of the ball screws of the four-bar-link actuation systems. The measured currents of the ankle, the knee, and the pelvis joints are illustrated in Fig. 23. Through these measurements, the payloads applied to the joints with respect to their postures are identified.

According to the measured data, the maximum payload current is 1.5 A in the ankle joint. Since the continuous maximum current of the 150 W Maxon motor is 6 A, it is validated that the joint actuation systems have enough capacity for 20 kg or over payloads. The reason for experiment of applying 13 kg payload is for safety of the robot. However, each step motion time is 1.1 s, which is somewhat slow and for much faster motions, the torque of the joint actuation system might need more torque. However, for the slow motions, the superior performance of the robot joint actuation system has been verified.

6. Conclusion

The analysis of the new 28-DOF humanoid robot, which can carry a 20 kg payload, has been presented. The pitching joint actuation systems for the arms and legs of the robot are designed using a closed-chain structure, based on the four-bar-link mechanism. An analysis of the closed-chain joint actuation systems of a very light arm, capable of handling heavy objects has been performed and the structure and forward kinematics of the robot, in addition to the four-bar-link structure of the joint actuation system have been analyzed. The leg of the robot is designed to support a 95 kg weight by the closed-chain joint actuation systems. Also, the dual arm of the humanoid robot is designed to be a very light 17 kg, but capable of handling 20 kg. For designing a light arm, FEM analysis has been performed using ANSYS, and the analysis on the kinematics and the structure of the arms and legs of the robot has been performed.

The superior performance of the humanoid robot, using the proposed closed-chain joint actuation systems, has been verified through successful walking experiments with a 85 kg load, and through experiments to support a 13 kg payload using the dual arm. Also, the capability of supporting a heavier payload of the joint actuation system of the robot has been verified through measuring the currents in the actuating motors of the leg and arm joints, so show that the loaded currents in the actuating motors are much less than the continuous maximum currents of the motors. Through experiments, it has been verified that the proposed humanoid robot, adopting the joint actuation systems of the closed-chain structure, has superior performance in walking with a heavy payload than demonstrated in previously developed humanoid robots.

Acknowledgments

This research was financially supported by the Ministry of Education, Science and Technology (MEST) and Korea Industrial Technology Foundation (KOTEF) through the Human Resource Training Project for Regional Innovation.

This research was supported by the Basic Science Research Program through the National Research Foundation of Korea (NRF) funded by the MEST (2010-0004372).

References

1. K. Hirai, M. Hirose, Y. Haidawa and T. Takenaka, "The Development of Honda Humanoid Robot," *Proceedings of the*

https://doi.org/10.1017/S0263574710000548 Published online by Cambridge University Press

IEEE International Conference on Robotics and Automation (1998) pp. 1321–1326.
2. http://world.honda.com/ASIMO/ (2009)
3. http://www.mstc.or.jp/hrp/main.html (2009)
4. K. Harada, S. Kajita, H. Saito, M. Morisawa, F. Kanehiro, K. Fujiwara, K. Kaneko, and H. Hirukawa, "A Humanoid Robot Carrying a Heavy Object," *Proceedings of the IEEE International Conference on Robotics and Automation* (2005) pp. 1724–1729.
5. J. Kim, I. Park, J. Lee, M. Kim, B. Cho and J. Oh, "System Design and Dynamic Walking of Humanoid Robot KHR-2," *Proceedings of the IEEE International Conference on Robotics and Automation* (2005) pp. 1443–1448.
6. M. Damme, F. Daerden and D. Lefeber, "A Pneumatic Manipulator used in Direct Contact with an Operator," *IEEE International Conference on Robotics and Automation* (2005) pp. 4505–4510.
7. J. P. Merlet, *Parallel Robots* (Kluwer Academic Publishers, Norwell, MA, 2000).
8. H. S. Choi and J. Oh, "A new revolute robot manipulator adapting the closed-chain mechanism," *J. Robot. Syst.* **22**(2), 99–109 (2005).
9. M. W. Spong and M. Vidyasagar, *Robot Dynamics and Control* (John Wiley & Sons, Hoboken, NJ, 1989).

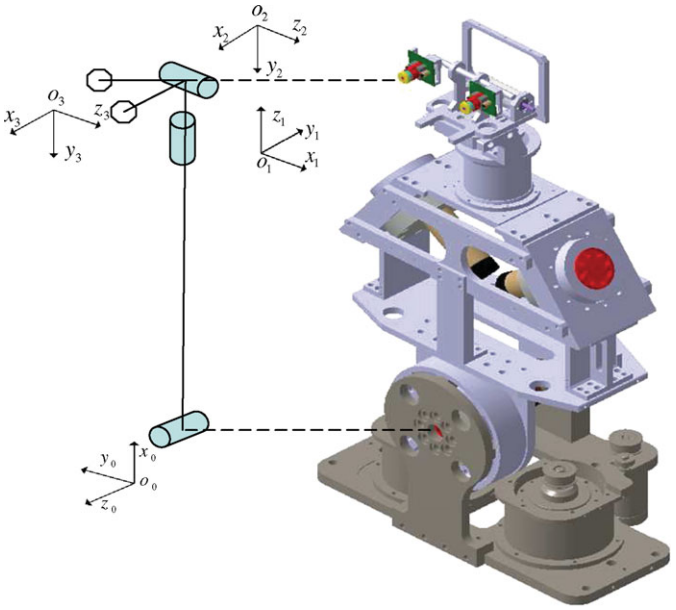

Fig. A1. D-H coordinates for the head.

Appendix

A1. Kinematics of the robot head

The position and orientation of the head are described with respect to the center of the robot body by using the homogeneous transformation matrix composed of the parameters in Table AI and matrix Eq. (A1).

$$A_i = R_{z,\theta} \cdot T_{z,d} \cdot T_{x,a} \cdot R_{x,\alpha} = \begin{bmatrix} C\theta_i & -S\theta_i \cdot C\alpha_i & S\theta_i \cdot S\alpha_i & a_i \cdot C\theta_i \\ S\theta_i & C\theta_i \cdot C\alpha_i & -C\theta_i \cdot S\alpha_i & a_i \cdot S\theta_i \\ 0 & S\alpha_i & C\alpha_i & d_i \\ 0 & 0 & 0 & 1 \end{bmatrix}. \quad \text{(A1)}$$

The homogeneous transformation matrix $T^3_{0,\text{head}}$ is expressed as follows:

$$T^3_{0,\text{head}} = A_1 A_2 A_3 = \begin{bmatrix} r_{11} & r_{12} & r_{13} & P_x \\ r_{21} & r_{22} & r_{23} & P_y \\ r_{31} & r_{32} & r_{33} & P_z \\ 0 & 0 & 0 & 1 \end{bmatrix}, \quad \text{(A2)}$$

where

$$\begin{aligned} r_{11} &= c\theta_1 c\theta_2 c\theta_3 - s\theta_1 s\theta_3, \\ r_{12} &= -c\theta_1 c\theta_2 s\theta_3 - s\theta_1 c\theta_3, \\ r_{13} &= -c\theta_1 s\theta_2, \end{aligned}$$

Table AI. Link parameters for the robot head.

Link	a_i	α_i	d_i	θ_i
1	0	90°	0	θ_1
2	0	−90°	d_2	θ_2
3	a_3	0	0	θ_3

$$\begin{aligned} r_{21} &= s\theta_1 c\theta_2 c\theta_3 + c\theta_1 s\theta_3, \\ r_{22} &= -s\theta_1 c\theta_2 s\theta_3 + c\theta_1 c\theta_3, \ r_{23} = -s\theta_1 s\theta_2 \\ r_{31} &= s\theta_2 c\theta_3, \ r_{32} = -s\theta_2 s\theta_3, \ r_{33} = c\theta_2, \\ P_x &= c\theta_1 c\theta_2 a_3 c\theta_3 - s\theta_1 a_3 s\theta_3 + s\theta_1 d_2, \\ P_y &= s\theta_1 c\theta_2 a_3 c\theta_3 + c\theta_1 a_3 s\theta_3 - c\theta_1 d_2, \\ P_z &= s\theta_2 a_3 c\theta_3. \end{aligned}$$

A2. Components of the homogeneous transformation matrix of the robot arm

$$\begin{aligned} r_{11} &= c_5\{c_1c_4(c_2c_3 - s_2s_3) - c_1s_4(s_2c_3 + c_2s_3)\} + s_1s_5, \\ r_{12} &= -s_5\{c_1c_4(c_2c_3 - s_2s_3) - c_1s_4(s_2c_3 + c_2s_3)\} + s_1s_5, \\ r_{13} &= c_1s_4(c_2c_3 - s_2s_3) + c_1c_4(c_2c_3 - s_2s_3), \\ r_{21} &= c_5\{s_1c_4(c_2c_3 - s_2s_3) - s_1s_4(s_2c_3 + c_2s_3)\} - c_1s_5, \\ r_{22} &= -s_5\{s_1c_4(c_2c_3 - s_2s_3) - s_1s_4(s_2c_3 + c_2s_3)\} - c_1c_5, \\ r_{23} &= s_1c_4(c_2c_3 - s_2s_3) + s_1c_4(s_2c_3 + c_2s_3), \\ r_{31} &= c_5\{c_4(s_2c_3 + c_2s_3) + s_4(c_2c_3 - s_2s_3)\}, \\ r_{32} &= -s_5\{c_4(s_2c_3 + c_2s_3) + s_4(c_2c_3 - s_2s_3)\} \\ r_{33} &= -c_4(c_2c_3 - s_2s_3) + s_4(s_2c_3 + c_2s_3), \\ P_x &= d_5\{s_1c_4(s_2c_3 + c_2s_3) + c_1s_4(c_2c_3 - s_2s_3)\} \\ &\quad + c_1(a_1 + a_2c_2 + a_3c_3c_2 - a_3s_3s_2), \\ P_y &= d_5\{s_1c_4(s_2c_3 + c_2s_3) + s_1s_4(c_2c_3 - s_2s_3)\} \\ &\quad + s_1(a_1 + a_2c_2 + a_3c_3c_2 - a_3s_3s_2), \\ P_z &= d_5\{s_4(c_3s_2 + c_2s_3) - c_4(c_2c_3 - s_2s_3)\} \\ &\quad + a_2s_2 + a_3s_3c_2 + a_3c_3s_2. \end{aligned}$$

https://doi.org/10.1017/S0263574710000548 Published online by Cambridge University Press

A3. Components of the homogeneous transformation matrix of the robot leg

$$
\begin{aligned}
r_{11} &= ((c\theta_2^* c\theta_3^* \theta_4^* - c\theta_2^* s\theta_3^* s\theta_4^*)c\theta_5^* \\
&\quad +(-c\theta_2^* c\theta_3^* s\theta_4^* - c\theta_2^* s\theta_3^* c\theta_4^*)s\theta_5^*)c\theta_6^* - s\theta_2^* s\theta_6^*, \\
r_{21} &= ((s\theta_3^* c\theta_4^* + c\theta_3^* s\theta_4^*)c\theta_5^* + (-s\theta_3^* s\theta_4^* + c\theta_3^* c\theta_4^*)s\theta_5^*)c\theta_6^*, \\
r_{31} &= ((s\theta_2^* c\theta_3^* c\theta_4^* - s\theta_2^* s\theta_3^* s\theta_4^*)c\theta_5^* \\
&\quad +(-s\theta_2^* c\theta_3^* s\theta_4^* - s\theta_2^* s\theta_3^* c\theta_4^*)s\theta_5^*)c\theta_6^* + c\theta_2^* s\theta_6^*, \\
r_{12} &= -((c\theta_2^* c\theta_3^* c\theta_4^* - c\theta_2^* s\theta_3^* \theta_4^*)c\theta_5^* \\
&\quad +(-c\theta_2^* c\theta_3^* s\theta_4^* - c\theta_2^* s\theta_3^* c\theta_4^*)s\theta_5^*)s\theta_6^* - s\theta_2^* c\theta_6^*, \\
r_{22} &= -((s\theta_3^* c\theta_4^* + c\theta_3^* s\theta_4^*)c\theta_5^* \\
&\quad +(-s\theta_3^* s\theta_4^* + c\theta_3^* c\theta_4^*)s\theta_5^*)s\theta_6^*, \\
r_{32} &= -((s\theta_2^* c\theta_3^* c\theta_4^* - s\theta_2^* s\theta_3^* s\theta_4^*)c\theta_5^* \\
&\quad +(-s\theta_2^* c\theta_3^* s\theta_4^* - s\theta_2^* s\theta_3^* c\theta_4^*)s\theta_5^*)s\theta_6^* + c\theta_2^* s\theta_6^*, \\
r_{13} &= (c\theta_2^* c\theta_3^* c\theta_4^* - c\theta_2^* s\theta_3^* s\theta_4^*)s\theta_5^* \\
&\quad -(-c\theta_2^* c\theta_3^* s\theta_4^* - c\theta_2^* s\theta_3^* c\theta_4^*)c\theta_5^*, \\
r_{23} &= (s\theta_3^* c\theta_4^* + c\theta_3^* s\theta_4^*)s\theta_5^* - (-s\theta_3^* s\theta_4^* + c\theta_3^* c\theta_4^*)c\theta_5^*, \\
r_{33} &= (s\theta_2^* c\theta_3^* c\theta_4^* - s\theta_2^* s\theta_3^* s\theta_4^*)s\theta_5^* \\
&\quad -(-s\theta_2^* c\theta_3^* s\theta_4^* - s\theta_2^* s\theta_3^* c\theta_4^*)c\theta_5^*,
\end{aligned}
$$

and the position vector for the end point is as follows:

$$
\begin{aligned}
p_x &= ((c\theta_2^* c\theta_3^* c\theta_4^* - c\theta_2^* s\theta_3^* s\theta_4^*)c\theta_5^* \\
&\quad +(-c\theta_2^* c\theta_3^* s\theta_4^* - c\theta_2^* s\theta_3^* c\theta_4^*)s\theta_5^*)c\theta_6^* a_6 - s\theta_2^* s\theta_6^* a_6 \\
&\quad +(c\theta_2^* c\theta_3^* c\theta_4^* - c\theta_2^* s\theta_3^* s\theta_4^*)c\theta_5^* a_5 + (-c\theta_2^* c\theta_3^* s\theta_4^* \\
&\quad -c\theta_2^* s\theta_3^* c\theta_4^*)s\theta_5^* a_5 c\theta_2^* c\theta_3^* c\theta_4^* a_4 + -c\theta_2^* s\theta_3^* c\theta_4^* a_4 \\
&\quad +c\theta_2^* c\theta_3^* a_3 + c\theta_2^* a_2 + a_1, \\
p_y &= ((s\theta_3^* c\theta_4^* + c\theta_3^* s\theta_4^*)c\theta_5^* + (-s\theta_3^* s\theta_4^* + c\theta_3^* c\theta_4^*)s\theta_5^*) \\
&\quad \times c\theta_6^* a_6 + (s\theta_3^* c\theta_4^* + c\theta_3^* s\theta_4^*)c\theta_5^* a_5 + (-s\theta_3^* s\theta_4^* \\
&\quad +c\theta_3^* c\theta_4^*)s\theta_5^* a_5 + s\theta_3^* c\theta_4^* a_4 + c\theta_3^* s\theta_4^* a_4 + s\theta_3^* a_3, \\
p_z &= ((s\theta_2^* c\theta_3^* c\theta_4^* - s\theta_2^* s\theta_3^* s\theta_4^*)c\theta_5^* + (-s\theta_2^* c\theta_3^* s\theta_4^* \\
&\quad -s\theta_2^* s\theta_3^* c\theta_4^*)s\theta_5^*)c\theta_6^* a_6 + c\theta_2^* s\theta_6^* a_6 + (s\theta_2^* c\theta_3^* c\theta_4^* \\
&\quad -s\theta_2^* s\theta_3^* s\theta_4^* c\theta_5^* a_5 + (-s\theta_2^* c\theta_3^* s\theta_4^* - s\theta_2^* s\theta_3^* c\theta_4^*) \\
&\quad \times s\theta_5^* a_5 + s\theta_2^* c\theta_3^* c\theta_4^* a_4 - s\theta_2^* s\theta_3^* s\theta_4^* a_4 + s\theta_2^* c\theta_3^* a_3 \\
&\quad +s\theta_2^* a_2 + d_1.
\end{aligned}
$$

https://doi.org/10.1017/S0263574710000548 Published online by Cambridge University Press